Research Article Vol. 59, No. 17 / 10 June 2020 / Applied Optics 5205

applied optics

# Optical method for micrometer-scale tracerless visualization of ultrafast laser induced gas flow at a water/air interface

Dashdeleg Baasanjav,[1,†] Javier Hernandez-Rueda,[1,2,†] Allard P. Mosk,[1] and Dries van Oosten[1,*]

[1]Debye Institute for NanoMaterials Science and Center for Extreme Matter and Emergent Phenomena, Utrecht University, Princetonplein 5, 3584 CC Utrecht, The Netherlands
[2]Kavli Institute of Nanoscience Delft, Department of Quantum Nanoscience, Delft University of Technology, Lorentzweg 1, 2628 CJ Delft, The Netherlands
*Corresponding author: D.vanOosten@uu.nl

Received 18 February 2020; revised 21 May 2020; accepted 24 May 2020; posted 26 May 2020 (Doc. ID 389542); published 9 June 2020

**We study femtosecond-laser-induced flows of air at a water/air interface, at micrometer length scales. To visualize the flow velocity field, we simultaneously induce two flow fronts using two adjacent laser pump spots. Where the flows meet, a stationary shockwave is produced, the length of which is a measure of the local flow velocity at a given radial position. By changing the distance between the spots using a spatial light modulator, we map out the flow velocity around the pump spots. We find gas front velocities near the speed of sound in air $v_s$ for two laser excitation energies. We find an energy scaling that is inconsistent with the Sedov–Taylor model. Due to the flexibility offered by spatial beam shaping, our method can be applied to study subsonic laser-induced gas flow fronts in more complicated geometries.** 

https://doi.org/10.1364/AO.389542

## 1. INTRODUCTION

Laser ablation is currently applied in research fields ranging from life-science to laser materials processing [1–4]. In particular, the use of femtosecond (fs) laser pulses is very appealing to induce ablation, mainly due to the ultrafast laser energy deposition and the extreme nonlinearity of the process [5–8]. These mechanisms have very distinct advantages, such as significantly reducing the heat-related collateral effects and achieving a subdiffraction limit spatial resolution [7]. Besides these technical advantages, the ultrafast nature of the laser excitation leads to a concatenation of several processes that are spread over different time scales, which is especially interesting to compartmentalize the problem. On the time scale of the order of the pulse duration, the laser energy is absorbed and a hot electron plasma is created. Depending on the photon energy and the electronic properties of the target, the absorption process can be mostly nonlinear (i.e., dielectrics, semiconductors) or linear (i.e., semiconductors, metals). For water (a dielectric) the initial absorption is due to multiphoton ionization and is therefore nonlinear. However, the excited electrons also induce linear absorption, through inverse bremsstrahlung and impact ionization [9,10]. On the picosecond time scale, the electrons thermalize with the atoms and molecules, which can lead to a phase change. In the specific example of water, this leads to the production of a volume of strongly supercritical water [9]. This volume will then rapidly expand, subjecting the target underneath to a strong recoil pressure, leading to liquid flow and potentially to splashing, on the microsecond time scale. To understand this liquid flow, it is of course paramount to know the initial thermodynamic conditions. To determine these initial conditions, the dynamics of the ablation plume expanding into the background gas needs to be fully understood. The dynamics during ultrafast ablation of liquids have been investigated using a number of time-resolved imaging methods, providing a wealth of information on the expansion of the plume [9–20]. However, the flow velocity of the gas that surrounds the expanding plasma cannot be directly visualized, as the length scales are far too small for traditional methods using tracer particles and the available time-resolved imaging techniques cannot resolve the subtle changes on the refractive index of the gas flow on the micrometer scale.

We recently reported on the generation and visualization of shockwaves at a water/air interface using multiple excitation spots in close proximity [21]. The resulting (opposing) gas flows produced at each irradiation spot can have a relative velocity exceeding the speed of sound, resulting in stationary shocks. These shocks give significant optical contrast in a reflectivity measurement, because they extend along the line of sight as

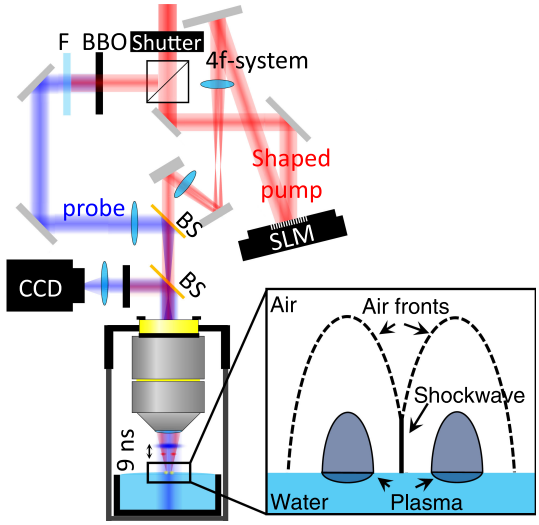


**Fig. 1.** Illustration of the experimental setup. Light from an amplified femtosecond laser is split into two paths. One path (pump, in red) is reflected on a spatial light modulator (SLM), shaping the phase of the beam. The surface of the SLM is imaged in the back focal plane of a microscope objective. The other path (probe, in blue) is first frequency doubled and focused in the back focal plane of the same microscope objective, leading to wide-field illumination. The pump-probe delay is set using a delay line in the probe path. The inset illustrates the geometry of the laser-excited water surface using a double pump.

illustrated in Fig. 1. In this work, we demonstrate the use of a spatial light modulator (SLM) to change the distance between the excitation spots on the fly. We use this method to investigate the radial dependence of the gas flow velocity around the excitation spots. We determine the local flow velocity by measuring the length of the resulting shockwaves and discuss energy dependence of the flow velocity field. Finally, we discuss future application of our method.

## 2. EXPERIMENTAL SETUP

In Fig. 1, we show a diagram of the setup. Laser pulses from an amplified fs laser (Hurricane, Spectra-Physics) with a duration of 150 fs and a wavelength of 800 nm are first split into a probe and a pump path using a polarizing beam splitter (PBS) and a lambda half-wave plate. For the experiments, we use a single laser shot that is picked using a mechanical shutter. The probe pulse is frequency doubled using a beta barium borate (BBO) crystal combined with a lambda half-wave plate, which is filtered in order to block the remaining IR laser light. Subsequently, we use a lens ($f = 200$ mm) to focus the probe beam in the back focal plane of a microscope objective (Nikon CFI60, 100×, N.A.0.8) to achieve wide field illumination. The pump beam is reflected on a SLM (Holoeye Pluto-BB for 700–1000 nm), which is used to imprint a phase pattern on the beam. This phase pattern is imaged in the back focal plane of the objective using two lenses in a $4f$ arrangement. We use phase maps of binary gratings that result in two dominant ($\pm 1$st) diffraction orders, resulting in two adjacent spots on the sample surface. By varying the period of the grating, we can vary the separation between the spots. The waist of the pump spots in the focus is 3.4 μm, which

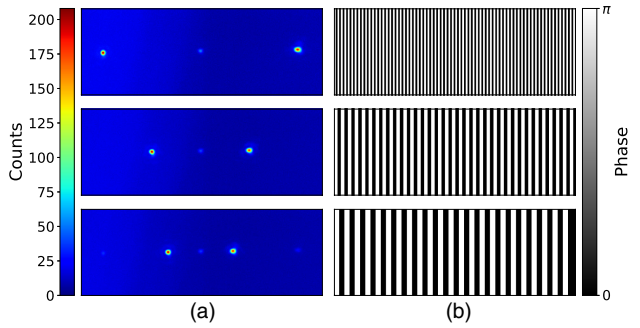


**Fig. 2.** (a) Typical intensity patterns achieved in an intermediate image plane. (b) Corresponding binary gratings displayed on the SLM.

for the pulse energies used in this work leads to an initial size of modification of 1.8 μm [20].

As a proof of principle, Fig. 2(a) shows typical illumination patterns recorded at the Fourier plane of the $4f$ system with highly attenuated fs laser pulses. Figure 2(b) shows the corresponding grating patterns displayed on the SLM. In all illumination patterns, a small amount of light can be seen in the center, corresponding to the zeroth order (specular) reflection of the SLM. Also, in the bottom image, weak higher-order spots can be seen. As long as these spots are sufficiently below the ablation threshold, they do not affect the measurements. The illumination patterns shown in Fig. 2(a) are imaged onto the surface of a sample that consists of 25 mL of milli-Q demineralized water. We control the energy of the pump pulse combining a lambda half-wave plate with a polarizing beam splitter. We measure the energy of the pump pulse right after the microscope objective in order to take into account losses throughout the experimental system. The light reflected from the water surface is collected by the objective. The reflected pump light is blocked by a bandpass filter ($400 \pm 10$ nm). The reflected probe light is used to image the laser-excited water/air interface by means of a tube lens (TL). The image is recorded using an electron multiplying CCD camera (Andor, Ixon 885). Note here that the light of a single laser probe pulse is recorded by the camera. In all experiments described in the work, we set the delay between the pump and the probe to 9 ns, as with this delay we make optimal use of our field of view (45 $\mu$m × 45 $\mu$m). We estimated the pulse duration stretching of the pump laser to be below 20 fs after passing through all the optical elements within the experimental setup.

## 3. TRANSIENT-REFLECTIVITY MEASUREMENT RESULTS

In Fig. 3, we display transient-reflectivity images obtained during the double-spot ablation process using several grating periods. For all images, we observe two dark disks at the laser excited locations. We attribute these to absorption and scattering of the probe light due to water droplets and clusters of molecules inside the ablation plume. Note that the initial size of the modification is (with a radius of 1.8 μm) significantly smaller than the black disks and the separation between them. We also observe ring-like features concentrically around these

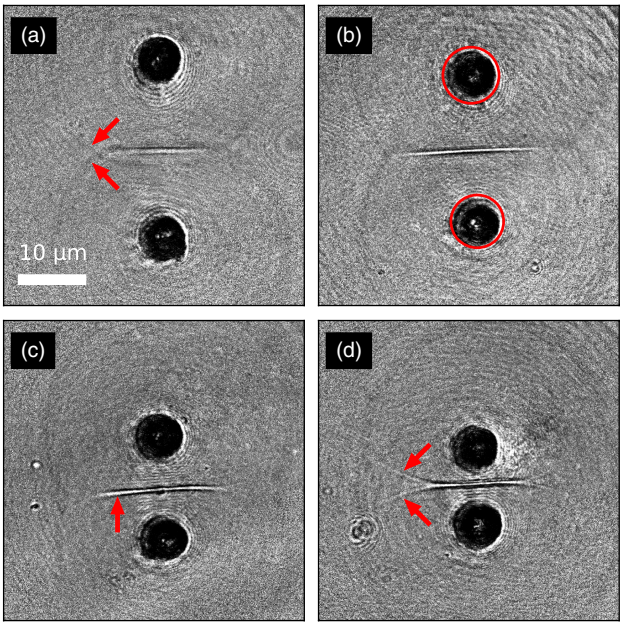


**Fig. 3.** Transient-reflectivity images obtained at a pump-probe delay of 9 ns and a fluence of 18 J/cm$^2$, for varying pump spot separation. The arrows in (a) points to weak shockwaves. The red circles in (b) illustrate the radius of the black regions as determined using a Hough transform. The arrows in (c) indicate the stationary shock caused by the opposing gas flow from the two excitation spots. The arrows in (d) show the bifurcation of the shockwave.

spots. These appear to be related to shockwaves in the surrounding air. We verified this by replacing the air above the water surface with helium, in which the rings are absent [20]. Most interestingly, we observe a strong stationary shock in between the two spots. This shockwave is caused by the fact that the opposing air flows resulting from the adjacent spots have a relative velocity that is strongly supersonic. With decreasing distance between the spots, the length of this stationary shock changes. In Fig. 3(c), we see that the stationary shock has a small curvature. This can be attributed to a slight imbalance in the energy of the two pulses as systematically demonstrated elsewhere [21]. Such an imbalance can, for instance, be caused by a slight tilt of the water surface produced by small vibrations. To assess the imbalance, the radii of the black regions are computed for each image using a Hough transformation (HoughCircles, OpenCV); see the red circumferences in Fig. 3(b).

For a given pulse energy, the average and standard deviation of all radii are calculated. Images in which both radii are within one standard deviation of the average are used in the rest of the analysis. In Fig. 3(d), we see that the stationary shock bifurcates at both ends. We can understand this as follows. When the gas flow reaches the shockwave, the increased local pressure causes the flow to partly deflect sideways. In the case of Fig. 3(d), the vapor and the shockwave are so close together that this deflection leads to a significant flow velocity component parallel to the stationary shock. This parallel flow adds to the radial flow, causing the flow to significantly exceed the speed of sound, resulting in the bifurcating tails of the stationary shockwave.

## 4. GAS FRONT VELOCITY ESTIMATION

In Fig. 4(a), we plot the length $L$ of the stationary shock as a function of $d$, where $2d$ is the distance between the centers of the excitation spots, for two peak fluences (18 J/cm$^2$ and 21 J/cm$^2$, both significantly above the breakdown fluence of 8.1 J/cm$^2$ [20]) on the sample surface. In the measurement of the length, we take into account only the straight section, discarding the bifurcating tails if they occur [as is the case in Fig. 3(d)]. The circled data points correspond to the images in Fig. 3 (the letter indicating the relevant subplot). We observe that as the distance between the pump spots is increased, the length of the shock grows until it reaches a maximum, after which it decreases again. The dashed vertical lines in the graph correspond to the distance at which we first observe the bifurcation of the shockwave. As can be seen, the occurrence of the bifurcation does not seem to significantly change the trend. Nevertheless, care should be taken when interpreting the results for shorter distances, as the bifurcation indicates a significant deflection of the flow.

As argued in [21], to observe these stationary shocks, the velocity from each excitation spot must be such that the component perpendicular ($v_\perp$) to the shock, shown in Fig. 4(c), is larger than half the velocity of sound ($v_s = 343$ m/s). In this way, the perpendicular components satisfy $v_\perp^{\text{up}} + v_\perp^{\text{down}} \geq v_s$. Therefore, the length $L$ of the stationary shock is determined by the point where $v_\perp = v_s/2$. At this position, the perpendicular velocity can be written as $v_\perp = vd/r$, where $r = \sqrt{d^2 + (L/2)^2}$ and $v$ is the radial flow velocity due to a single excitation spot. From this equation and the above criterion, we find that $L = 2d\sqrt{4(v/v_s)^2 - 1}$. In other words, for a constant velocity $v$, the length of the shockwave increases with increasing separation. However, for larger separation, the radially expanding flow will only just have reached the halfway point between

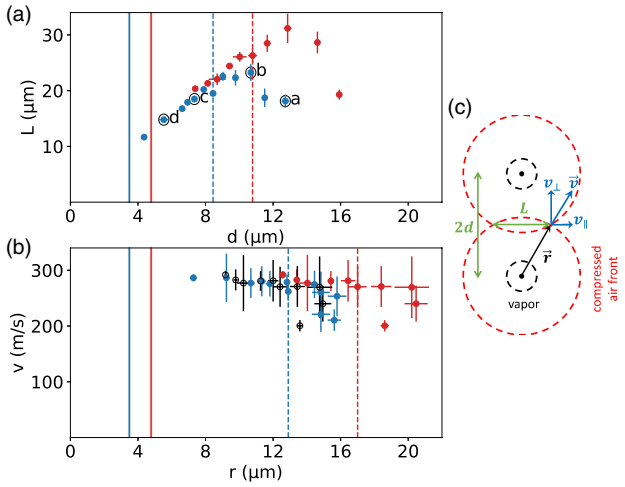


**Fig. 4.** (a) Shockwave length as a function of distance $d$ between pump and the shockwave, for 18 J/cm$^2$ (blue) and 21 J/cm$^2$ (red). The dashed vertical lines indicate the distance below which bifurcation of the stationary shock is observed. The circled data points correspond to the typical images in Fig. 3, the letter indicating the relevant subplot. (b) Corresponding velocity as a function of radial distance $r$. The solid vertical lines indicate the radius of the black disk in the images. The open black symbols are the data for 21 J/cm$^2$ with the scaled $r$ axis, such that the points best overlap with the data for 18 J/cm$^2$. (c) Geometrical scheme of the double pulse excitation.

the two excitation spots, causing a decrease in length for larger separation. Rewriting the above equation, we find that the velocity can be written as follows:

$$v = v_s \frac{\sqrt{4d^2 + L^2}}{4d}. \quad (1)$$

This equation is used to convert the length into a radial velocity. The result of this conversion is shown in Fig. 4(b), in which the velocity $v$ is a function of the radius $r$. For a spot separation of 14 μm ($d = 7$ μm) and a fluence of 18 J/cm$^2$, we find a velocity of 280 ± 27 m/s. This value is in agreement with our previously reported results on the ultrafast laser ablation dynamics of water using double-beam illumination at a single separation distance [21]. Note also that, as the measured velocity of the gas flow is lower than the velocity of sound, it would not have resulted in optical contrast in transient-reflectivity images in a single-spot experiment. We see that, as expected, the radial velocity decreases as a function of the radial distance $r$. We also see that, surprisingly, the radial velocity seems almost independent of the incident pulse energy. Note that for large spot separations, the radius $r$ appears to decrease again. This is an artifact caused by the downturn of the length $L$ for large $d$, which was discussed above. Beyond the maximum in $L$, the results plotted in Fig. 4(b) are therefore unreliable. The solid vertical lines in the graphs mark the average radius of the black regions in Fig. 4 and, as before, the dashed vertical lines correspond to the distance where we first observe bifurcation of the shock, indicating the point where deflection of the flow becomes important. For shorter distances, Eq. (1) therefore underestimates the local flow velocity; these velocities should thus be considered a lower limit to the actual velocity.

The black circles in Fig. 4(b) are the data for 21 J/cm$^2$ but with $r$ scaled down by a factor 1.36 ± 0.07 (corresponding to the ratio of the radii of the black regions for the two energies), leaving the velocity unscaled. The fact that the datasets for 18 J/cm$^2$ and 21 J/cm$^2$ (corresponding to $E_1 = 3.4$ μJ and $E_2 = 4.0$ μJ per spot, respectively) then collapse onto each other suggests an approximately quadratic scaling with incident energy [as $(E_2/E_1)^m \approx 1.37$ with $m = 1.9 \pm 0.3$]. However, the relevant energy for the gas flow is the absorbed rather than the incident energy. We therefore need to take into account how the absorbed energy depends on the incident energy. In transparent materials, the light absorption is in the first order mediated by multiphoton ionization and avalanche ionization, which scale with different powers of the incident laser intensity, $I^n$ and I, respectively. If we consider only multiphoton absorption, the order of the process $n$ is defined as the number of laser photons needed to overcome the ionization potential of water $U/\hbar\omega = 6$, where $U = 9.5$ eV [18] and $\hbar\omega = 1.56$ eV. We could thus assume that the absorbed energy $E_{abs}$ scales as $E_{abs} \propto E^6$, with $E$ the incident energy. In contrast, tunnel ionization would lead to a linear dependence. However, under our experimental conditions, the Keldysh parameter is approximately 0.8, which means tunnel ionization will be important but not dominant. Finally, we should also take into account the effect of avalanche ionization. Therefore, we run a full calculation of the deposited energy within the irradiated water volume by using a finite-difference time-domain algorithm combined with the multiple rate equations method (MRE) as we recently reported [9]. From the simulation, we find that the ratio of absorbed energies, given the pulse energies used in the experiment, is ∼1.29, whereas the ratio of the pulse energies is ∼1.18. This suggests a scaling of $E_{abs} \propto E^n$, with $n \sim 1.5$, as opposed to the power 6 we naively assumed on the basis of the multiphoton ionization. Using this result, we find that the quadratic scaling in the incident energy corresponds to a scaling with the absorbed energy to the power of 1.3 ± 0.2, rather than the $E_{abs}^{1/3}$ scaling one might expect on the basis of the Sedov–Taylor solution for a three-dimensional point blast model [22]. Obviously, a full study of the energy scaling behavior would require experiments at significantly more laser energies. Yet, these results already lay bare a) the obvious limitations of applying the Sedov–Taylor model to an expansion that is not necessarily self-similar and b) the need to account for both linear and nonlinear excitation.

## 5. CONCLUSION AND OUTLOOK

In summary, we demonstrate the use of a spatial light modulator to visualize the light-induced-flow velocity field during ultrafast laser ablation. We have reconstructed the fs-laser-induced air flow velocity profile for two different excitation energies. We find that the flow velocity is almost independent of the laser pulse energy, but that the radial scale of the velocity field depends approximately quadratically on the laser pulse energy. By computing the absorbed energy as a function of the incident pulse energy, considering both nonlinear and linear laser excitation using an MRE model, we show that such an energy scaling is incompatible with a Sedov–Taylor-like behavior, illustrating the limitations of applying the Sedov–Taylor model in this context. The use of a SLM opens up the possibility of creating exotic illumination patterns that would lead to more complex effects. For instance, a toroidal excitation pattern would lead to converging gas flow on the liquid/gas interface. One can envision the use of such converging shockwaves to focus an ablation plume, which might have application in pulsed laser deposition. Furthermore, our method of flow visualization using a SLM can readily be applied in such illumination geometries.

**Funding.** H2020 Marie Skłodowska-Curie Actions (703696 ADMEP); Nederlandse Organisatie voor Wetenschappelijk Onderzoek (VICI 68047618).

**Acknowledgment.** The authors thank Cees de Kok, Paul Jurrius, and Dante Killian for technical support.

**Disclosures.** The authors declare no conflicts of interest.

[†]These authors contributed equally to this paper.

## REFERENCES

1. R. R. Gattass and E. Mazur, "Femtosecond laser micromachining in transparent materials," Nat. Photonics **2**, 219–225 (2008).
2. U. K. Tirlapur and K. König, "Targeted transfection by femtosecond laser," Nature **418**, 290–291 (2002).
3. Z. Nagy, A. Takacs, T. Filkorn, and M. Sarayba, "Initial clinical evaluation of an intraocular femtosecond laser in cataract surgery," J. Refract. Surg. **25**, 1053–1060 (2009).

4. J. Hernandez-Rueda, J. Siegel, M. Galvan-Sosa, A. R. de la Cruz, M. Garcia-Lechuga, and J. Solis, "Controlling ablation mechanisms in sapphire by tuning the temporal shape of femtosecond laser pulses," J. Opt. Soc. Am. B **32**, 150–156 (2015).
5. B. Rethfeld, "Unified model for the free-electron avalanche in laser-irradiated dielectrics," Phys. Rev. Lett. **92**, 187401 (2004).
6. B. Rethfeld, "Free-electron generation in laser-irradiated dielectrics," Phys. Rev. B **73**, 035101 (2006).
7. P. Balling and J. Schou, "Femtosecond-laser ablation dynamics of dielectrics: basics and applications for thin films," Rep. Prog. Phys. **76**, 036502 (2013).
8. B. H. Christensen and P. Balling, "Modeling ultrashort-pulse laser ablation of dielectric materials," Phys. Rev. B **79**, 155424 (2009).
9. J. Hernandez-Rueda and D. van Oosten, "Transient scattering effects and electron plasma dynamics during ultrafast laser ablation of water," Opt. Lett. **44**, 1856–1859 (2019).
10. T. Winkler, C. Sarpe, N. Jelzow, L. L. Lillevang, N. Götte, B. Zielinski, P. Balling, A. Senftleben, and T. Baumert, "Probing spatial properties of electronic excitation in water after interaction with temporally shaped femtosecond laser pulses: experiments and simulations," Appl. Surf. Sci. **374**, 235–242 (2016).
11. R. R. Krueger, J. S. Krasinski, C. Radzewicz, K. G. Stonecipher, and J. J. Rowsey, "Photography of shock waves during excimer laser ablation of the cornea: effect of helium gas on propagation velocity," Cornea **12**, 330–334 (1993).
12. T. Juhasz, X. H. Hu, L. Turi, and Z. Bor, "Dynamics of shock waves and cavitation bubbles generated by picosecond laser pulses in corneal tissue and water," Lasers Surg. Med. **15**, 91–98 (1994).
13. C. B. Schaffer, N. Nishimura, E. N. Glezer, A. M.-T. Kim, and E. Mazur, "Dynamics of femtosecond laser-induced breakdown in water from femtoseconds to microseconds," Opt. Express **10**, 196–203 (2002).
14. A. Vogel and V. Venugopalan, "Mechanisms of pulsed laser ablation of biological tissues," Chem. Rev. **103**, 577–644 (2003).
15. I. Apitz and A. Vogel, "Material ejection in nanosecond Er:YAG laser ablation of water, liver, and skin," Appl. Phys. A **81**, 329–338 (2005).
16. C. Sarpe, J. Köhler, T. Winkler, M. Wollenhaupt, and T. Baumert, "Real-time observation of transient electron density in water irradiated with tailored femtosecond laser pulses," New J. Phys. **14**, 075021 (2012).
17. B. Strycker, M. Springer, A. Traverso, A. Kolomenskii, G. Kattawar, and A. Sokolov, "Femtosecond-laser-induced shockwaves in water generated at an air-water interface," Opt. Express **21**, 23772–23784 (2013).
18. N. Linz, S. Freidank, X.-X. Liang, H. Vogelmann, T. Trickl, and A. Vogel, "Wavelength dependence of nanosecond infrared laser-induced breakdown in water: evidence for multiphoton initiation via an intermediate state," Phys. Rev. B **91**, 134114 (2015).
19. T. T. Nguyen, R. Tanabe, and Y. Ito, "Comparative study of the expansion dynamics of laser-driven plasma and shock wave in in-air and underwater ablation regimes," Opt. Laser Technol. **100**, 21–26 (2018).
20. J. Hernandez-Rueda and D. van Oosten, "Dynamics of ultrafast laser ablation of water," arXiv preprint arXiv:1810.06946 (2018).
21. M. Vreugdenhil, D. van Oosten, and J. Hernandez-Rueda, "Dynamics of femtosecond laser-induced shockwaves at a water/air interface using multiple excitation beams," Opt. Lett. **43**, 4899–4902 (2018).
22. L. I. Sedov, *Similarity and Dimensional Methods in Mechanics* (CRC Press, 1993).